

Cancellation of crossflow instabilities through multiple discrete roughness elements forcing

Giulia Zoppini , Theodoros Michelis, Daniele Ragni, and Marios Kotsonis
Delft University of Technology, Delft 2629HS, The Netherlands



(Received 25 April 2022; accepted 2 November 2022; published 28 December 2022)

The presented work introduces a cancellation technique, based on the linear superposition of stationary crossflow instabilities (CFIs) through the application of a streamwise series of optimally positioned discrete roughness element (DRE) arrays on a swept wing surface. The DRE arrays are designed and arranged with suitable amplitude and phase shift to induce velocity disturbance systems that destructively interact, ultimately damping the developing CFIs. The robustness of this technique is investigated for a smooth wing surface as well as in the presence of enhanced distributed surface roughness. The resulting flow fields are measured with infrared thermography and particle tracking velocimetry, allowing for the extraction of the laminar-to-turbulent transition front location and for the characterization of the local boundary layer development. The acquired data show that the superposition of suitably arranged DRE arrays can successfully suppress monochromatic CFIs, reducing their amplitude and growth and delaying the boundary layer transition to turbulence when applied on a smooth wing surface. However, the presence of elevated background roughness significantly reduces the effectiveness of the proposed method.

DOI: [10.1103/PhysRevFluids.7.123902](https://doi.org/10.1103/PhysRevFluids.7.123902)

I. INTRODUCTION

The laminar to turbulent transition of swept wing boundary layers (BLs) subject to a favorable pressure gradient is dominated by the development of crossflow instabilities (CFIs) [1–3]. In low freestream turbulence environments, such as free flight, the dominant instability develops in the form of stationary corotating vortices approximately aligned with the freestream flow [1]. These vortices grow along the wing chord, and through their inductive action deform the BL by displacing momentum in the wall-normal direction. The resulting spanwise and wall-normal shears are receptive to secondary, high-frequency instabilities whose rapid growth is ultimately responsible for the flow transition to turbulence [3–5].

The onset and development of stationary CFIs is highly sensitive to surface roughness [2,6]. In particular, even in the case of highly polished wall surfaces, the residual distributed roughness of the wing locally affects the developing CFIs through receptivity processes. Therefore, many experimental and numerical works apply an artificial forcing in the form of arrays of discrete roughness elements (DREs) periodically distributed along the wing span [2,3,6–8]. The application of such arrays, usually located in the vicinity of the leading edge, enhances the spanwise uniformity of the BL by focusing the developing CFIs on a single monochromatic mode with a spanwise wavelength corresponding to the elements inter-spacing. In most research applications, the forced

Published by the American Physical Society under the terms of the [Creative Commons Attribution 4.0 International](https://creativecommons.org/licenses/by/4.0/) license. Further distribution of this work must maintain attribution to the author(s) and the published article's title, journal citation, and DOI.

wavelength corresponds to the naturally most unstable crossflow mode (λ_{crit}). However, previous investigations showed that forcing a subcritical mode (i.e., $\lambda < \lambda_{\text{crit}}$) excites an artificial set of CFIs, hindering the growth of the naturally most unstable modes and delaying the laminar-to-turbulent BL transition up to 9% chord [8]. Nonetheless, despite the successful transition delay obtained in wind tunnel experiments, subsequent works found that subcritical forcing is highly sensitive to the external flow conditions (i.e., distributed roughness and freestream turbulence), especially in a free-flight environment. Specifically, investigations by Woodruff *et al.* [10], Carpenter *et al.* [9], and Saric *et al.* [11] extended wind tunnel tests to in-flight experiments, observing a more unpredictable and irregular behavior for the subcritical forcing technique. Throughout these works, numerous roughness configurations have been investigated, combining subcritical forcing with both smooth (i.e., with surface roughness rms equivalent to $R_q = 0.3$ and $2.2 \mu\text{m}$ median peak-to-peak) and rough (i.e., $R_q \simeq 1.7\text{--}6$ and $7\text{--}31.4 \mu\text{m}$ median peak-to-peak) surface finishing. Overall, only a few of the considered configurations provided a transition delay in the order of 4–5 % chord, while repeatable and robust trends were not established. The majority of tested configurations caused transition advancement or showed no measurable effect, especially for the rougher surface finishing cases.

The subcritical forcing technique has also been investigated through direct numerical simulation (DNS) studies. Specifically, the DNS base flow is artificially deformed at the numerical domain inlet, introducing a wall-normal velocity component with finite amplitude and fixed subcritical spanwise periodicity [upstream flow deformation (UFD) [5]]. This technique focuses the energy and phase of the developing instabilities on the forced CFI mode, inhibiting the development of both critical primary and secondary instabilities through nonlinear interactions and mean flow distortion (MFD). By focusing the disturbance on a single mode, UFD succeeds in fixing the position and phase of the developing crossflow vortices with respect to the wing surface. Therefore, this technique can improve the performance of flow control methods, which make use of the destructive interference between velocity disturbance systems [12]. In particular, DNS investigations showed that the application of a series of successive spanwise rows of suction orifices can successfully control the BL development if the constructive interference of the three-dimensional (3D) disturbances induced by each row is minimized [13]. Additionally, the combination of UFD with classical BL suction allows for the optimal arrangement of the suction holes location with respect to the developing CFI [14]. This allows for the application of optimally arranged, strong localized suction to already nonlinear CFI configurations, successfully inhibiting the onset of secondary instabilities [14]. The practical implementation of BL suction remains technically complicated and costly, however the considered numerical investigations obtained a noteworthy transition delay (in the order of 10% chord or more [13]). Another concept based on the implementation of destructive interference as a control technique is the cancellation of Tollmien-Schlichting (TS) waves in a 2D BL. The linearly growing TS instabilities have been successfully attenuated by superimposing artificially generated monofrequency disturbances with properly adjusted amplitude and phase shift [15–18].

Given its significant effect on the flow development, the investigation of distributed (i.e., random) roughness in 2D-BL has attracted growing interest in recent years [19–23]. In these works, the wing surface roughness was enhanced through the application of distributed roughness patches (DRPs), inducing BLs that are locally affected by the roughness geometrical features. The local DRP higher peaks proved to be the main drivers for the origin of low-speed, high-vorticity, and high-shear regions [22]. Moreover, the symmetry of the peak shape is responsible for the topology of the near-peak flow field: a pair of counter-rotating vortices forms if the peak shape resembles a symmetrical DRE, while a single vortex develops if the peak resembles an asymmetric element placed at an angle in the flow field [22]. The resulting BL contains multiple CFI modes, partly losing the flow-field uniformity and transition front regularity typical of DRE forced boundary layers [24]. Additionally, minimal changes in the incurred CFI amplitude and development are observable when the DRPs are modified by removing the embedded valleys [23]. This result lends utility to the present investigation, in which the applied DRPs only protrude from the wing surface. Finally, the considered studies also identified that a DRP composed of only the highest peaks obtained by

removing the surrounding foothills leads to enhanced BL disturbances. The beneficial effect given by the presence of the foothills is defined as *roughness shielding* [25]. This effect can be linked to the enhanced thickness of the BL developing over a DRP [23], as well as to a process of energy redistribution driven by the presence of the distributed roughness [26].

Further investigations have been dedicated to the shielding phenomena resulting from the superposition of isolated discrete roughness elements and a DRP patch in a 2D-BL [26–28]. These investigations showed that the presence of the sole DRP induces smaller disturbances when compared to the flow field incurred by the isolated DRE or the combination of the two roughness systems. Moreover, minimal differences were identified between the last two configurations regarding the emerging disturbances amplitude, energy, and overall development. Additionally, these works showed that two purposely isolated DREs optimally applied at subsequent chord locations can effectively reduce the incurred disturbances amplitude and delay the BL transition with respect to the single DRE forcing.

Based on the aforementioned observations, the present work introduces a technique for the cancellation of CFI instabilities developing in a 3D boundary layer. This is based on the linear superposition of stationary CFIs introduced by the application of a streamwise series of optimally positioned DRE arrays. In particular, the reduction of the CFI amplitude and the resulting BL transition delay can be achieved thanks to the destructive interference of the velocity disturbances introduced by the streamwise successive arrays, when these are appropriately adjusted in amplitude and spanwise phase shift. Such a forcing configuration is compatible with the cancellation of CFI developing in a realistic free-flight scenario. Specifically, given the residual distributed surface roughness of common swept wings, the naturally developing BL is typically dominated by the simultaneous development of a set of CFI modes, with *a priori* unknown phase and wavelength. Therefore, the application of a *reference* DRE array is expected to condition the developing flow field by focusing the instabilities into a monochromatic CFI mode [2,6], while damping the BL spectral content associated with the other excited wavelengths [5]. This results in a flow scenario comparable to that obtained by UFD. Accordingly, successive DRE arrays (named *control* arrays in the remainder of this work) can be optimally arranged and applied at more downstream chord locations in order to dampen the introduced monochromatic CFI through linear destructive interference.

The main purpose of this experimental investigation is to map the effect of multiple DRE arrays in canceling CFIs artificially introduced by a reference array. Comparably to previous investigations, the reference DRE array is applied to force the most unstable CFI mode (λ_1 [2,3,29]). The control arrays are then designed with a different amplitude and suitable phase shift in order to introduce velocity disturbances that linearly superimpose and dampen the preexisting CFI. Forcing the critical CFI mode differs from the traditional flow control applications, in which DRE arrays or UFD force a subcritical wavelength (typically of $2/3\lambda_1$) [5,8]. This design choice is based on the desire to investigate the cancellation capabilities of the sole linear superposition of the reference critical CFI and the control velocity disturbance systems. Nevertheless, the proposed control method can be expected to work also for other than the critical forced wavelengths. The incurred flow fields are measured through infrared (IR) thermography, delivering a global estimate of the transition location, and through particle tracking velocimetry (PTV), locally describing the time-averaged BL velocity field.

The first part of this work investigates the cancellation of monochromatic CFI developing on a smooth wing surface (i.e., $R_q = 0.2 \mu\text{m}$ and an average height of $5 \mu\text{m}$). However, the typical distributed surface roughness for commercial air vehicles is represented by an average height of $11 \mu\text{m}$ [30]. Hence, to extend the applicability of the proposed technique to more realistic transition scenarios, the present work additionally investigates the multiple DRE arrays effect on the developing CFI in the presence of enhanced distributed surface roughness. Randomized distributed roughness is obtained by spraying an adhesive compound directly on the wing surface. The applied patches and the incurred flow fields are assessed to ensure the repeatability of the forced BL dominant features. Multiple DRE configurations, comparable to the ones measured for the smooth wing surface, are then applied on the wing. In such a scenario, the reference array is expected to

focus the set of CFI modes excited by the DRP into a single monochromatic instability, in a process similar to UFD. This results in a fixed CFI periodicity and phase, possibly damping the BL spectral content associated with the smaller wavelength induced by the DRP [5]. As such, the application of successive control arrays enables the cancellation of the monochromatic CFI induced by the DRP-reference array combination. The interaction between the disturbance systems introduced by various DRP and DRE arrays, as well as the resulting flow features, are measured through IR and PTV.

II. METHODOLOGY

A. Wind tunnel and wing model

The measurements presented in this work are performed on an in-house designed, constant-chord swept wing model (M3J [31]). This wing is designed to investigate the development of primary and secondary CFIs, which dominate the BL evolution and transition [3]. The model is placed in the low-speed low turbulence wind tunnel (LTT) at the TU Delft, an atmospheric closed return tunnel developing a test section flow characterized by low freestream turbulence ($T_u/U_\infty \simeq 0.025\%$ [32]). Acquisitions are performed on the wing pressure side for a fixed angle of attack ($\alpha = -3.36^\circ$) and varying freestream Reynolds number [$\text{Re}_{c_x} = (1.9\text{--}2.9) \times 10^6$].

Two different coordinate systems are used throughout this work: the first is integral to the wind tunnel floor, with spatial components X, Y, Z and velocity components U, V, W ; the second is integral to the swept wing, with the z -axis aligned to the leading edge, spatial components x, y, z , and velocity u, v, w .

B. Discrete roughness elements

In experimental investigations on CFIs, the discrete-roughness-element (DRE) array is usually located close to the wing leading edge, i.e., in the vicinity of the first neutral point of the forced mode [1,3,6]. Previous investigations identified that the most unstable CFI mode for the current setup is $\lambda_1 = 8$ mm [32,33]. Numerical stability solutions computed by using an in-house developed linear stability solver (LST [32,34]) indicate that the λ_1 wavelength corresponds to the most amplified mode (or to one of the most amplified modes) throughout the whole Re_{c_x} range considered. Additionally, recent investigations conducted by the authors demonstrated that a downstream shift of the forcing array location (i.e., $x_{\text{DRE}}/c = 0.125$) induces CFIs with smaller initial amplitude while keeping the near-element flow topology almost unaltered [35]. These downstream configurations, however, provide easier measurement access to near-element flow field, thanks to the naturally increased BL thickness.

The DRE arrays are manufactured in-house by CNC laser cutting of a 0.1 mm nominal thickness self-adhesive black PVC foil. Elements of nominal height $k_1 = 0.1$ mm and $k_2 = 0.2$ mm are used throughout the presented investigation. The higher elements are obtained by pasting multiple layers of foil on top of each other prior to cutting. The inter-spacing of the elements corresponds to λ_1 , while detailed geometrical parameters are reported in Ref. [35] (table 2).

The measurements presented in this work aim at investigating the cancellation of CFIs as an effect of the superposition of the flow structures introduced by multiple successive DRE arrays. Preliminary investigations conducted by the authors drove the design of the forcing configurations measured in the present study. In particular, the flow field induced by a reference array of critically spaced DREs located at $x_{\text{DRE}}/c = 0.15$ was measured through tomographic PTV, identifying the main near-element flow structures and their orientation in the flow field [36]. This provides a measure of the existing constant phase angle between the near-wake structures and the freestream flow ($\simeq 6^\circ$), which in turn allows for proper computation of the required shift between the reference (A_R) and the following control (A_C) array. The chordwise shift between the two arrays is set to $x/c = 0.02$, sufficiently extended for the damping of the initial transient and the emergence of modal stationary CFI. As such, the velocity disturbances introduced by A_C superpose to the CFI induced

TABLE I. Geometrical parameters of measured forcing configurations. Individual DRE arrays (A_n , forcing mode λ_1) and DRP patches (D_n). IR acquisitions for all reported cases for $Re_{cx} = (1.9-2.9) \times 10^6$. PTV acquisitions for selected cases for $Re_{cx} = 2.17 \times 10^6$.

Case	DRE/DRP	k	x_{DRE}/c	Re_k	k/δ^*	x_{DRP}/c
C1-	A_1	0.2	0.125	94	0.44	
	A_2	0.2	0.145	89	0.40	
	A_3	0.2	0.165	87	0.39	
	A_4	0.2	0.185	85	0.37	
C2-	A_1	0.2	0.1	101	0.49	
	A_2	0.2	0.12	95	0.44	
	A_3	0.2	0.14	90	0.41	
	A_4	0.2	0.16	88	0.39	
C3-	A_1	0.2	0.1	101	0.49	
	A_2	0.1	0.12	22	0.22	
C4-	A_1	0.1	0.1	23	0.24	
	A_2	0.2	0.12	94	0.44	
C5-	A_1	0.2	0.1	101	0.49	
	A_2	0.2	0.13	93	0.42	
	A_3	0.2	0.125	94	0.44	
	A_4	0.2	0.155	88	0.39	
C6-	A_1	0.2	0.075	113	0.29	
	A_2	0.2	0.095	102	0.49	
C7-	D_1-D_{11}					0
	D_{13}					0.035
C8-	A_1	0.1	0.02	42	0.57	
	A_2	0.1	0.04	32	0.38	
	A_3	0.1	0.05	30	0.35	
	A_4	0.1	0.075	26	0.28	
	A_5	0.1	0.095	23	0.25	
	A_6	0.1	0.1	24	0.24	
	A_7	0.1	0.125	22	0.21	
	A_8	0.1	0.145	21	0.20	
	D_I					0
	D_{II}					0.035
C9-	A_1	0.2	0.05	127	0.35	
	A_2	0.2	0.07	113	0.29	
	D_I					0
C10-	A_1	0.1	0.125	22	0.21	
	A_2	0.2	0.145	89	0.41	
	A_3	0.2	0.165	87	0.39	
	D_{II}					0.035

by A_R , without interacting with the complex flow structures dominating the near-DRE flow field [29,35,37]. The control array application is designed with a spanwise shift such that its elements are located in correspondence with the evolving CF vortices induced by A_R . Moreover, an additional spanwise phase shift of $\lambda_1/2$ is introduced between the two DRE arrays in order to superpose high-(low-) speed regions induced by A_R to low- (high-) speed regions induced by A_C . Further control arrays are added with the same chordwise spacing and no phase shift with respect to A_C , only accounting for the crossflow vortex tilt with respect to the freestream flow.

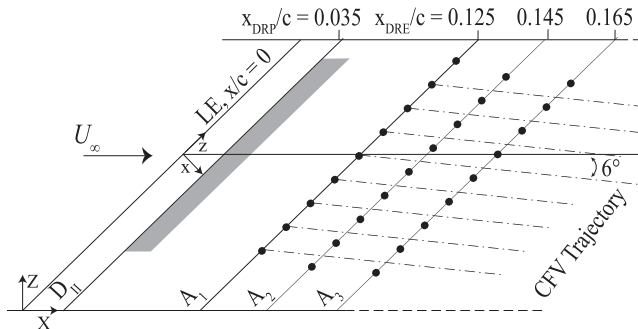


FIG. 1. Sketch of multiple DRE array and DRP patch application for forcing case C10 (not to scale).

The main configurations discussed in the present work are reported in Table I. The multiple array forcing cases are built by combining a reference array and one or more control arrays. Individual DRE arrays are indicated as A_n , and feature specific characteristics collected in Table I. The sketch reported in Fig. 1 additionally shows the multiple arrays forcing geometrical arrangement for a representative case. Both the effect of individual arrays (i.e., case C1-A₁) and multiple arrays forcing (i.e., case C1-A₁₋₃ given by the superposition of reference array A_1 and control arrays A_2 and A_3) are investigated and discussed in Sec. III.

C. Distributed roughness patches

To extend the applicability of the introduced technique to more realistic transition scenarios, it is desirable to evaluate its cancellation capabilities under conditions of elevated background roughness. To enable this, the wing surface roughness is enhanced by applying random distributed roughness patches (DRPs), mimicking the effect of a rough wing surface finishing. These patches are obtained by applying a rectangular mask on the wing surface extending for $x/c = 0.03$, and spraying the corresponding portion of the model with a layer of spray adhesive. DRPs are applied at various chord locations between the leading edge (i.e., $x_{\text{DRP}}/c = 0$) and $x_{\text{DRP}}/c = 0.125$.

As each patch contains a random distribution of local roughness peaks, multiple DRP configurations are measured during this campaign. To characterize the geometrical features of the patches, a subset of the applied DRP is scanned with a scanCONTROL 30xx profilometer operating with a semiconductor laser having a 405 nm wavelength and 1.5 μm reference resolution. The scanned domain extends for $x/c = 0.02$, acquiring the spanwise DRP amplitude signal (k_{DRP}) at various x/c . With this procedure the average and peak k_{DRP} , the DRP spanwise wavelength content, and the repeatability of its geometrical features are estimated. In particular, Fig. 2(a) indicates that the average k_{DRP} of a roughness patch (averaged in the spanwise and streamwise directions) is $k_{\text{DRP}} \simeq 0.012 \pm 0.005$ mm. The average height of the considered DRP is comparable with previous experimental investigations (see, e.g., Refs. [9,11]), as well as with civil aviation applications [30]. However, the local roughness height can reach isolated peak values of $\simeq 0.18$ mm, comparable to the amplitude of the applied DRE elements.

The spanwise spectral content of the patches is investigated by applying a spatial fast Fourier transform (FFT) to the acquired spanwise amplitude signal. The spectra extracted at a representative x/c location, corresponding to half of the DRP extent, are reported in Fig. 2(b). The spanwise spectral content in the DRP shape indicates that its geometrical features are described by a set of spanwise wavelengths distributed within the $0-\lambda_1/2$ range. As such, the DRP patches are expected to excite a set of CFI modes with various spanwise wavelengths distributed within the same range. These forcing conditions lead to the development of a BL containing a set of simultaneously developing small wavelengths CFI (Sec. IV [38]). Finally, Figs. 2(c) and 2(d), respectively, report a sketch of the representative DRP patch as reconstructed from the acquired profilometer data, and

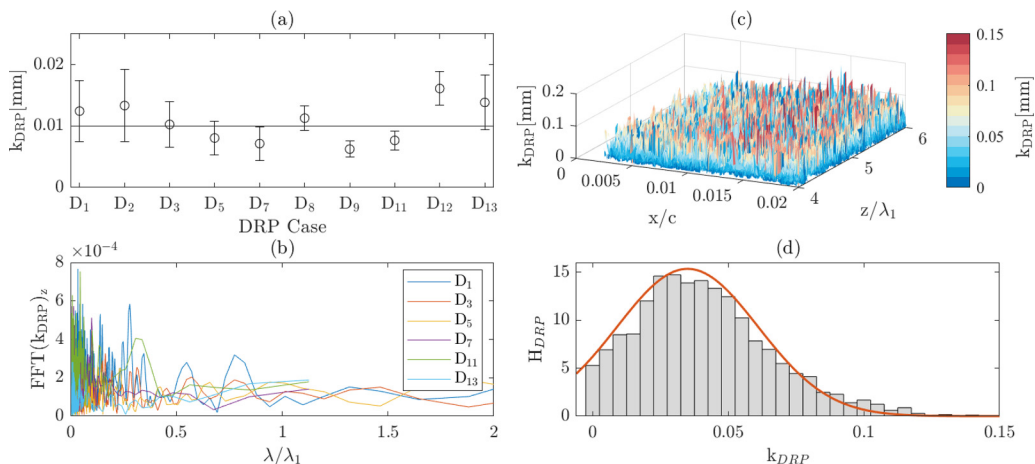


FIG. 2. (a) Height and (b) wavelength content of various DRP patches (Table I). Reconstruction of a region of the C7- D_8 roughness patch (c) from the acquired profilometer data and (d) from the local heights histogram H_{DRP} . Probability density function plot for a normal distribution with a mean of 0.035 and a standard deviation of 0.026 (red line).

the corresponding local heights histogram. Given the overall repeatability of the DRP geometrical features, the flow field induced by individual patches is investigated in Sec. IV, confirming that the dominant flow features are mostly independent of the local patch geometry. As such, the investigation of the interaction between the velocity disturbance systems induced by the DRP and the DRE arrays is only performed accounting for two representative DRP patches: D_I located at the leading edge, and D_{II} located at $x_{DRP}/c = 0.035$. The flow features resulting from the superposition of DRP and DRE arrays are discussed in Sec. V.

The DRP and DRP-DRE configurations discussed in the current work are reported in Table I (i.e., cases C7–C10). The measured DRP patches are indicated as D_n , while the configurations resulting from the superposition of DRP and DRE are, for example, indicated as C10- D_{II} - A_{1-3} . This case forces the BL flow with DRP patch D_{II} , reference array A_1 , and control arrays A_2 and A_3 . Figure 1 sketches the geometrical arrangement of the roughness elements of case C10, featuring the simultaneous application of a DRP patch and multiple DRE arrays.

D. Measurement techniques and data analysis

1. Infrared thermography

Infrared (IR) thermography is a nonintrusive measurement technique based on the Reynold's analogy [39] that images the wing surface temperature providing a global overview of the BL evolution. Specifically, IR images indicate whether laminar-to-turbulent BL transition occurs, as higher temperature regions are associated with laminar flow (i.e., regions of low wall shear), while lower temperature regions correspond to turbulent flow (i.e., regions of high shears) [1,24,32].

An Optris PI640 IR camera images the model pressure side (i.e., the wing side corresponding to the highest integrated pressure) for the chosen range of Re_{c_x} at $\alpha = -3.36^\circ$. The acquired domain covers the whole wing chord, and is centered at the wing midspan with a spatial resolution of $\simeq 1.7$ mm/px. To reduce the image-to-noise ratio, for each measured case 80 images are collected at a frequency of 4 Hz and are averaged. Additionally, external surface heating through IR-optimized halogen lamps (3×400 and 2×500 W) improves the thermal contrast between the laminar and turbulent BL regions. Throughout the presented measurement, the influence of the external model heating on the transition location is considered to be negligible. In fact, the model temperature modifications compared to the reference flow temperature, i.e., T_m/T_f , always lay within the 1–1.04

range, which previous experimental investigations identify as noninfluential on the BL transition location [40].

The averaged IR images are geometrically mapped to the tunnel-attached Cartesian framework (X, Y, Z) and are postprocessed through an in-house developed routine based on the differential infrared thermography (DIT) approach [41,42]. The transition front location is identified as the location of the maximum gradient of the DIT image [41]. A linear fit of the locally identified transition location is performed along the wing span, and is controlled through 95% confidence bands. The resulting chordwise estimate is considered as representative for the BL laminar-to-turbulent transition location (x_{TR}).

2. Planar particle tracking velocimetry

Planar particle tracking velocimetry (PTV) acquisitions provide a local quantification of the BL flow and its chordwise evolution, highlighting the effects of the considered forcing configurations on the developing CFI.

Throughout this work, the PTV flow fields are acquired in the zy plane (i.e., the spanwise wall-normal plane). The wall-normal direction is nondimensionalized as $y/\bar{\delta}^*$, where $\bar{\delta}^* \simeq 0.75$ mm is the experimental displacement thickness of the natural BL (i.e., no DRE applied) at $x/c = 0.25$. The PTV domain is centered at the wing midspan and extends for $z/\lambda_1 \simeq 4$ and $y/\bar{\delta}^* \simeq 3.5$. The BL development in the zy plane is described by the spanwise and wall-normal time-averaged velocity components, namely \bar{w} and \bar{v} , respectively.

The flow is illuminated using a Quantel Evergreen Nd:YAG dual cavity laser (200 mJ pulse energy at $\lambda = 532$ nm). Through suitable optics, the laser beam is manipulated in a sheet aligned to the zy plane (i.e., inclined at 45° to the freestream direction). One LaVision Imager camera (sCMOS, 2560×2160 pixels, 16-bit, $6.5 \mu\text{m}$ pixel pitch) equipped with a 200 mm lens and a $2\times$ teleconverter images the flow field. This optical arrangement results in a 400 mm focal lens with numerical aperture $f_\# = 8$, corresponding to a magnification ratio of 0.47 and a resolution of $\simeq 73$ px/mm. The BL is resolved up to the wall vicinity ($\bar{w}/W_\infty = 0.09\%$, with W_∞ being the local freestream velocity in the z direction). The laser and camera are mounted on an automated traversing system, which shifts them in unison allowing acquisition of various chordwise PTV planes while maintaining proper alignment and focus. Planes between 15% and 35% of the chord are measured with a laser thickness of approximately 1 mm. The flow is seeded through a SAFEX fog generator, dispersing $\simeq 0.5 \mu\text{m}$ droplets of a water-glycol mixture in the wind tunnel.

For each plane, 2000 image pairs are acquired at a frequency of 10 Hz and time interval between pairs of 15 μs , corresponding to a freestream particle displacement of $\simeq 18$ pixels. Each image pair is processed in LaVision Davis 10 through a two-frame PTV algorithm to identify the particle trajectories in the acquired plane. Binning and conversion to a Cartesian grid of the obtained particle tracks are also performed through Davis, resulting in a final window of 8×8 pixels corresponding to a vector spacing of approximately 0.11 mm along the y and z directions. The velocity uncertainty within the BL reaches an average value of 1.5% of the local velocity. The wall location is identified through an in-house developed MATLAB routine as the maximum light reflection region in the raw particle images.

Further processing of the time-averaged velocity fields is performed to extract the main flow features. The spanwise-average of \bar{w} , performed at each y -location, provides an estimate of the wall-normal BL mean velocity profiles (\bar{w}_b). By subtracting the \bar{w}_b profile to \bar{w} , the disturbance velocity field is obtained (\bar{w}_d). The root mean square (rms) of the spanwise velocity signal can instead provide an estimation of the disturbance profile along the y -direction ($\langle \bar{w} \rangle_z$) (see, e.g., Refs. [7,43,44]). Additionally, a spatial FFT is performed to infer the spectral organization of the flow field: at each y -coordinate, the spanwise \bar{w} signal is transformed in the spatial frequency domain [$\text{FFT}_z(\bar{w})$], providing information on the modal composition of the developing BL and on the chordwise evolution of the individual Fourier modes for different forcing configurations. Moreover, for each acquired PTV plane, the local CFI amplitude (A_{int}) is estimated following the

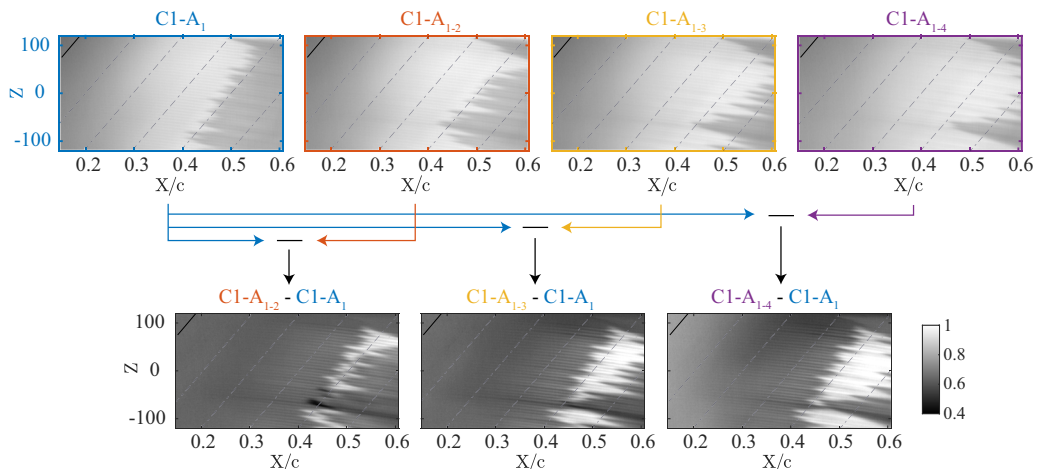


FIG. 3. IR acquisitions at $Re_{cx} = 2.27 \times 10^6$ for forcing case C1. Upper row: IR images for C1-A₁, C1-A₁₋₂, C1-A₁₋₃, and C1-A₁₋₄ configurations. Bottom row: DIT images computed subtracting the C1-A₁ case to the multiple array cases. Wing leading edge (full black line); flow comes from the left.

integral amplitude definition [45]. Namely, the disturbance profiles $\langle \bar{w} \rangle_z$, or the FFT shape functions corresponding to a single mode, are integrated along y up to $y = \delta_{99}$ to quantify the CFI chordwise evolution.

III. EFFECT OF MULTIPLE DRE ARRAYS FORCING

A. Effect of multiple DRE arrays on transition

The baseline configuration discussed in the following analysis is case C1-A₁₋₄, composed of four DRE arrays of height k_2 spaced at $\lambda/\lambda_1 = 1$ (Table I). The reference array C1-A₁ is located at $x_{DRE}/c = 0.125$, while the control arrays are placed at successive intervals of 2% chord downstream. As discussed in Sec. II B, the first control array C1-A₂ is arranged to have a phase shift of $\lambda_1/2$ with respect to A₁, while control arrays C1-A₃ and C1-A₄ are in phase with C1-A₂.

IR images are acquired for the considered range of Re_{cx} starting from the reference array configuration (C1-A₁) and progressively adding the control arrays. The resulting images for case C1 at $Re_{cx} = 2.27 \times 10^6$ are reported on the top row of Fig. 3, while DIT images computed by subtracting the C1-A₁ data to the multiple array cases are reported in the bottom row. The brighter portion of the DIT images is indicative of the transition delay achieved through the multiple array forcing. Significant transition delay is already obtained by applying a single control array (i.e., C1-A₂). Nonetheless, the cumulative effect given by the addition of control arrays C1-A₃ and C1-A₄ shifts the BL laminar-to-turbulent transition further downstream.

A quantitative estimation of the transition front chordwise location (x_{TR}/c) and, therefore, of the achieved transition delay is obtained as discussed in Sec. II D 1. This procedure is performed for each considered forcing configuration within the acquired Re_{cx} range. The resulting transition locations are reported in Fig. 4(a), showing the achieved transition delay is robust to the mild modifications of Re_{cx} considered in this work. Figure 4(a) indicates that the considered multiple array forcing case (C1-A₁₋₄) significantly affects the developing BL, delaying the transition front location up to 8% chord downstream. The first two control arrays applied (i.e., C1-A₂ and C1-A₃) play a major role in achieving this result, nonetheless array C1-A₄ is contributing to a further downstream shift of the transition location especially for the higher Re_{cx} considered. The transition delay obtained by applying multiple DRE arrays is comparable with the 9% transition delay observed by Saric *et al.* [8] in the first experimental investigations dedicated to subcritical

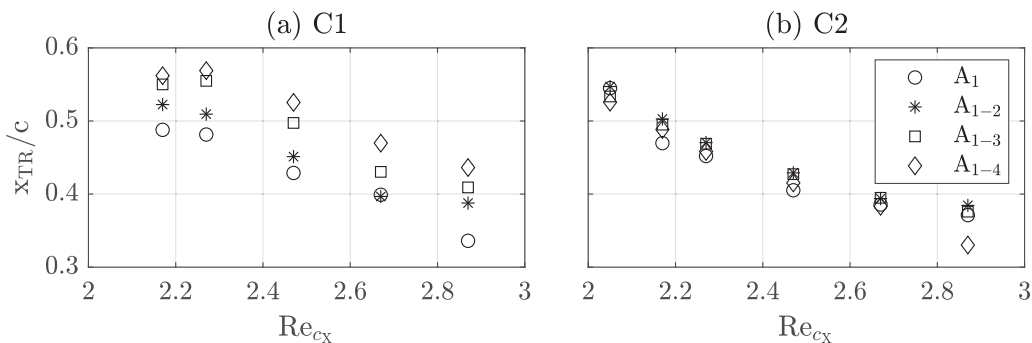


FIG. 4. Transition front chordwise location at various Re_{cx} for cases (a) C1 and (b) C2.

roughness forcing. Nonetheless, successive investigations [9,11] already outlined the sensitivity of the employed technique to external disturbances such as freestream turbulence or distributed surface roughness, resulting in reduced control capabilities. This aspect is further addressed in Sec. V.

B. Linearity of the disturbances superposition

To better understand and characterize the underlying flow mechanisms, the flow field resulting from the superposition of arrays of case C1 is further investigated through the PTV acquisitions. Figure 5 reports the disturbance (\bar{w}_d) and time-averaged (\bar{w}) velocity contours for the reference array forcing (C1- A_1) and for the multiple array forcing (C1- A_{1-4}) at two representative chord forcing locations. The BL resulting from forcing configuration C1- A_1 [Figs. 5(a) and 5(b)] is clearly modulated by the development of a typical CFI, showing the periodic alternation of high- and low-speed regions along the spanwise direction [1–3]. Both the geometric size of the developing crossflow vortices, as well as the CFI intensity, are reduced by the application of multiple control arrays [C1- A_{1-4} , Figs. 5(d) and 5(e)], correlating well with the observed delay in transition. Furthermore,

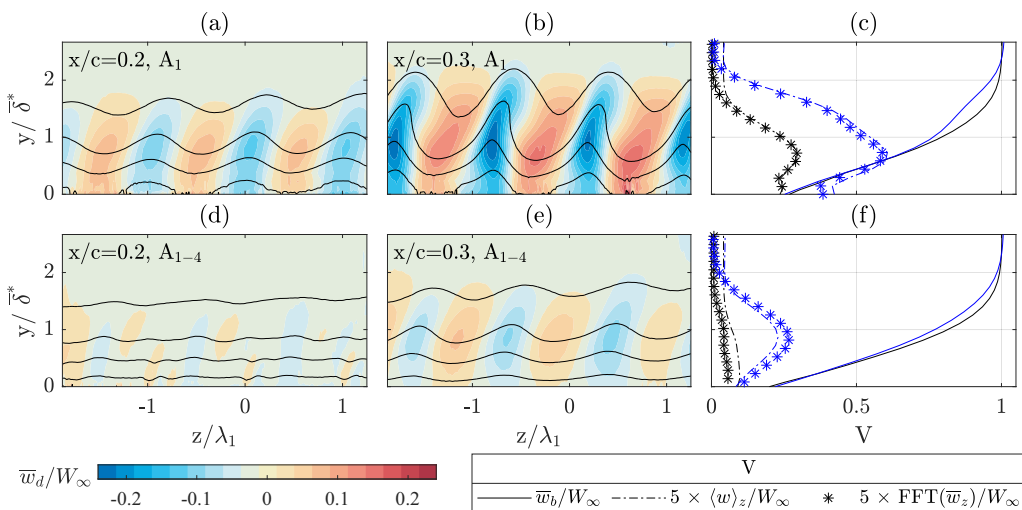


FIG. 5. Contours of \bar{w}_d at (a), (d) $x/c = 0.2$ and (b), (e) $x/c = 0.3$ for configurations (a), (b) C1- A_1 and (d), (e) C1- A_{1-4} . Contours of \bar{w} every $20\%W_\infty$ (black solid lines). (c), (f) Comparison of \bar{w}_b (solid line), $\langle w \rangle_z$ (dash-dotted line), and λ_1 FFT shape function (*) at $x/c = 0.2$ (black lines) and $x/c = 0.3$ (blue lines).

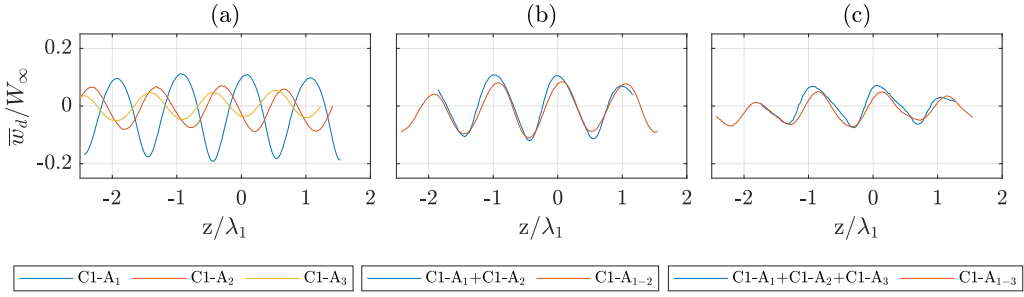


FIG. 6. Spanwise \bar{w}_d signal at $x/c = 0.25$ and $y/\delta^* = 0.5$ for (a) C1-A₁, C1-A₂, C1-A₃; (b) the summation of C1-A₁, and C1-A₂ (blue line) and C1-A₁₋₂ (red line); (c) the summation of C1-A₁, C1-A₂, and C1-A₃ (blue line) and C1-A₁₋₂₃ (red line).

the $\langle w \rangle_z$ wall-normal evolution [Figs. 5(c) and 5(f)] indicates that the significant CFI amplitude reduction obtained by applying the control arrays prevents the development of nonlinearities. In fact, the weak secondary peak visible in the $\langle w \rangle_z$ profile at $x/c = 0.3$ for case C1-A₁ is absent in case C1-A₁₋₄. Additionally, by hindering the CFI evolution, the flow field resulting from the DRE array superposition is reducing the deformation of the mean flow. This is indicated by the absence of the inflection point in the \bar{w}_b profile at $x/c = 0.3$ for forcing case C1-A₁₋₄ [Fig. 5(f)].

The CFI amplitude reduction and the consequent transition front delay are achieved thanks to the linear superposition of the velocity disturbance systems introduced by each of the applied arrays. This affects the CFI in their initially linear development phase, reducing their onset amplitude and downstream growth. To verify the assumption of linear superposition, the summation of the velocity disturbances induced by each of the individual arrays applied in case C1 is compared to the disturbances measured aft of the multiple arrays configuration. PTV acquisitions of the flow field incurred by individual arrays are performed for cases C1-A₁, C1-A₂, C1-A₃. For sake of simplicity, the spanwise disturbance velocity signal \bar{w}_d is extracted at a single x - and y -location corresponding to $x/c = 0.25$ and $y/\delta^* = 0.5$. The spanwise velocity signal extracted from the flow fields originated by each individual array is reported in Fig. 6(a). The spanwise phase shift imposed to the velocity signals corresponds to the geometrical spanwise shift imposed between subsequent arrays of case C1-A₁₋₄. Figures 6(b) and 6(c), respectively, compare the summation of the velocity signals for the first two and three arrays to the velocity disturbances measured in the multiple arrays flow fields (i.e., configurations C1-A₁₋₂ and C1-A₁₋₃). The reported velocity signals are comparable both in trend and amplitude, confirming the linearity of the superposition effect.

A spatial FFT is applied to the spanwise time-averaged PTV velocity signal to investigate the BL spectral content and identify the dominant stationary CFI and their chordwise evolution. Considering the baseline forcing case C1, the spectral analysis of the reference array configuration (C1-A₁) and of the four array configuration (C1-A₁₋₄) is reported in Figs. 7(a) and 7(b). As expected, the application of the sole reference array results in a monochromatic flow field focused on the λ_1 mode, Fig. 7(a). The excited CFI rapidly grows throughout the domain, accompanied by the second ($\lambda_2 = \lambda_1/2$) and third ($\lambda_3 = \lambda_1/3$) harmonics, which appear successively downstream. The development of higher harmonics confirms the presence of nonlinearities in the evolution of the BL forced by C1-A₁, in agreement with the weak secondary peak identified in $\langle \bar{w} \rangle_z$ [Fig. 5(c)]. Figure 7(b) indicates that the BL incurred by the multiple array forcing configuration is also dominated by the development of the λ_1 mode. However, in the case C1-A₁₋₄ the CFI spectral amplitude is significantly reduced, to the point that no harmonics are detected. This agrees well with the absence of measurable nonlinear interactions and the reduced flow distortion observed for this forcing case [Fig. 5(f)]. Additionally, the FFT shape functions are compared to the $\langle w \rangle_z$ profiles in Figs. 5(c) and 5(f). A good match in both shape and maximum amplitude is observed, suggesting

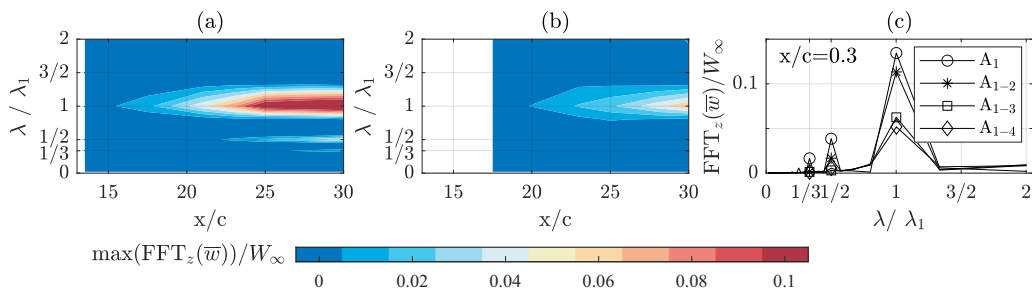


FIG. 7. Spatial FFT analysis for case C1. Fourier spectra contours in the x - λ plane for (a) C1- A_1 and (b) C1- A_{1-4} . (c) Fourier spectra at $x/c = 0.3$ and $y/\delta^* = 1$ for C1 configurations.

that the λ_1 Fourier mode is sufficient to correctly describe the dominant CFI within the considered BL region. In fact, as also indicated by the spectra reported in Fig. 7(c), the λ_1 mode harmonics are still relatively weak (for case C1- A_1) or even below the measurement resolution threshold (for case C1- A_{1-4}) within the considered domain. It is noteworthy that the CFI dominant wavelength is left unaltered by the array superposition. This further confirms that the CFI cancellation is the result of the linear superposition of the reference CFI and the velocity disturbances introduced by the applied control arrays, rather than being driven by the introduction of nonlinear interactions as is the case for the UFD technique [5,8,11].

Further characterization of the BL flow field resulting from the array superposition is given by the estimation of the amplitude of the developing CFI instabilities [45]. In particular, the integral amplitudes (A_{int}) are estimated by integrating the $\langle w \rangle_z$ profile along the y -direction, up to $y = \delta_{99}$. Comparable amplitude calculations can be obtained by integrating the FFT shape function corresponding to one specific mode (i.e., wavelength), estimating amplitudes of individual harmonics, such as λ_1 and λ_2 (i.e., A_{int,λ_1} and A_{int,λ_2} , respectively), excluding all other flow disturbances. The resulting amplitude values are reported in Figs. 8(a)–8(c) as extracted for the reference array configuration C1- A_1 and for the multiple arrays forcing C1- A_{1-2} , C1- A_{1-3} , and C1- A_{1-4} . The A_{int} describing the CFI evolution for the flow field forced by the sole reference array C1- A_1 is almost double with respect to the amplitudes pertaining to the CFI developing in the multiple array forcing cases. Moreover, only mild differences can be observed between A_{int} and corresponding A_{int,λ_1} , confirming the prevalent role of the dominant λ_1 mode on the flow-field development for all forcing

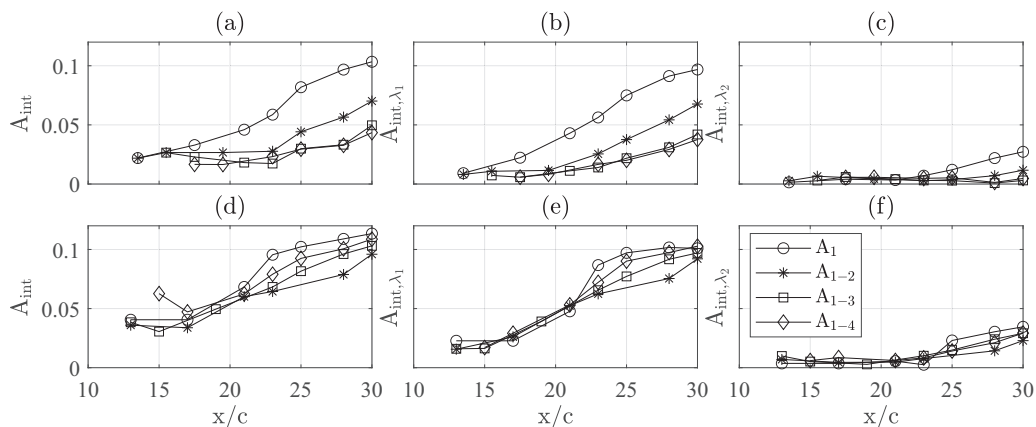


FIG. 8. Integral amplitudes chordwise evolution for cases (a)–(c) C1 and (d)–(f) C2. (a), (d) A_{int} ; (b), (e) A_{int,λ_1} ; (c), (f) A_{int,λ_2} .

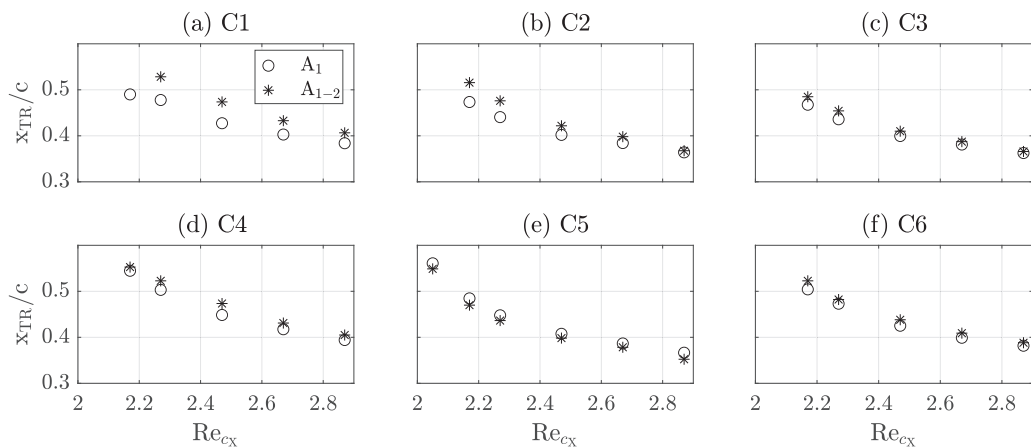


FIG. 9. Transition front chordwise location at various Re_{cx} for various forcing cases. Refer to Table I for the specifics of each forcing case considered.

configurations of case C1. With the single array forcing, amplitude saturation is reached at the end of the acquired domain, accompanied by the growth of the λ_2 harmonics, as shown by Fig. 8(c). The cumulative effect of the control arrays superposition leads instead to significant amplitude reduction: amplitude saturation is no longer reached for the multiple DRE forcing cases, and the λ_2 harmonics retains almost null values. Results presented in Figs. 8(d)–8(f) are discussed in the following Sec. III C 3.

Throughout the considered configurations, the unsteady perturbation development is left mainly unaltered by the DRE array superposition. Reduced primary instability amplitudes correspond to later development or to weaker unsteady disturbances. Nonetheless, in all considered cases the BL transition occurs due to the development of secondary instabilities and their rapid breakdown, as previously observed by multiple investigations [3,5]. Given that these considerations are well-established within the CFI investigation and development, no extended treatment of the unsteady disturbance development is included in the present work.

C. Sensitivity to DRE arrays parameters

To ensure the robustness of the DRE superposition technique in cancelling the CFI introduced by the reference array, a range of configurations of double arrays (A_R and A_C) with different design and arrangement is measured. This parametric investigation is performed through IR acquisitions while modifying the x_{DRE} location, the chordwise spacing of the arrays, and the DRE height. The analysis of these cases is limited to the extraction of the transition front location for the acquired Re_{cx} range, reported in Fig. 9. The effects of the three considered parameters, namely the DREs amplitude, chordwise spacing, and chord location, are discussed hereafter.

1. Effect of DRE amplitude

Forcing configurations composed by a reference array and a control array of height k_2 successfully delay BL transition when arranged with a 2% chordwise distance and a phase shift of $\lambda_1/2$ [i.e., C1- A_{1-2} , C2- A_{1-2} , Figs. 9(a) and 9(b)]. However, comparable configurations built using DRE arrays of smaller amplitudes (i.e., k_1) reduce the effectiveness of the multiple DRE forcing technique. This can be associated with the excessively high or insufficiently low amplitude of the velocity disturbances introduced by the control array with respect to the reference CFI. As an example, case C3- A_{1-2} is presented in Fig. 9(c). For this forcing configuration, A_1 features DRE of amplitude k_2 , while A_2 is designed with nominal DRE amplitude of k_1 . Therefore, the control

array induces velocity disturbances that are too weak to effectively cancel the existing reference CFI. This results in minor changes of the transition front location. Configuration C4-A₁₋₂ shows instead the opposite effect, as the control array induces velocity disturbances that are too strong, thus effectively “overshooting” the reference CFI. Also this configuration results in a mild delay of the transition front location [Fig. 9(d)].

2. Effect of arrays chordwise spacing

Forcing configurations composed by a reference and a control array arranged at a chordwise spacing of $x/c = 0.03$ result in reduced cancellation capabilities with respect to case C1-A₁₋₂. This effect is possibly due to the superposition of the velocity disturbances introduced by A_C to already too strong CFI forced by the A_R , resulting in a transition advancement [i.e., C5-A₁₋₂ or C5-A₃₋₄, Fig. 9(e)]. In fact, in their initial phases of development, the modal CFIs follow an exponential growth process, rapidly overgrowing the control velocity disturbances introduced by A_C .

A shorter chordwise spacing between the reference and control array (i.e., $x/c = 0.01$, not reported for the sake of brevity) also leads to an upstream shift of the transition location. This can be related to the application of A_C in a region affected by flow structures pertaining to the element near-wake evolution. Therefore, the velocity instabilities introduced by the control array interact with complex flow structures that evolve into modal CFIs only further downstream [29,35].

3. Effect of arrays chord location

Reference DRE arrays located in the vicinity of the wing leading edge are expected to introduce stronger CFI, advancing the BL transition [11,35]. Nonetheless, case C2 shows that the multiple arrays forcing technique is capable of cancelling the CFI incurred by a reference array located at $x_{DRE}/c = 0.1$. As indicated in Table I, the multiple array design of case C2 is identical to the design of case C1, except for the more upstream x_{DRE}/c . Figures 4(b) and 8(d)–8(f) confirm that the application of control arrays (i.e., configuration C2-A₁₋₄) is capable of hindering the development of the CFI introduced by C2-A₁. The effect of the first applied control array significantly delays the BL transition and reduces the CFI amplitude. However, the more upstream location of the application is reducing the cancellation capabilities of the multiple DRE arrays technique. Accordingly, the addition of further control arrays with the same design as case C1 appears to be detrimental for the transition location and CFI amplitude evolution.

If shifted towards more upstream chord locations, the combination of the reference and control arrays has the undesired effect of advancing the transition front [i.e., C6-A₁₋₂, Fig. 9(c)]. This is attributed to the excessively high initial amplitude of the disturbances introduced by the reference array, as well as to the rapid exponential growth of the CFI at these chord locations, which may be affected by the stronger pressure gradient typical of the LE region, making the applied array design inefficient [35]. Ideally, arrays of smaller amplitudes and relative displacement placed at upstream chord locations (i.e., $x_{DRE}/c \leq 0.075$) may effectively delay transition. Fabrication of repeatable and robust DREs of lower height than used in the present study is deemed essential for the evaluation of such cases.

The considerations reported beforehand indicate that the multiple arrays design parameters (i.e., DRE height, chordwise distance, x_{DRE}/c , and arrays phase shift) are fundamental for the successful cancellation of the CFI introduced by the reference array. However, the results presented so far only consider the cancellation of a monochromatic CFI introduced in the BL. As such, a further step is taken to investigate the robustness and capabilities of the proposed cancellation technique by simulating the elevated surface roughness finishing of a realistic wing, which typically leads to the development of multiple randomly spaced and phased CFI modes in the BL. The resulting flow field and its interaction with the velocity disturbances introduced by multiple DRE configurations are discussed hereafter.

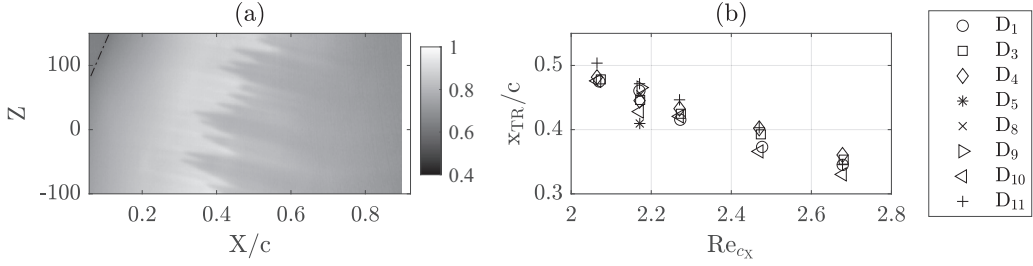


FIG. 10. (a) IR acquisition at $Re_{cx} = 2.17 \times 10^6$ for forcing case C7-D₈. (b) Transition front chordwise location at various Re_{cx} for DRP of case C7.

IV. EFFECT OF DRP PATCHES FORCING

A. Effect of DRP on transition and CFI

Random distributed roughness is applied on the swept wing surface using patches of sprayed adhesive. Given the need to investigate several combinations of DRE and DRP forcing, these patches were applied *in situ*, measured, and then removed. The repeatability of the various DRE geometry has been assessed in Sec. II C, nevertheless the flow field forced by the DRP is hereafter investigated to ensure no considerable variations appear among the different measured cases.

The dominant flow topology is characterized for a representative DRP located at the wing leading edge (C7-D₈, Table I). A global overview of the flow field induced by C7-D₈ is acquired through IR measurements [Fig. 10(a)]. The sawtooth pattern of the transition front appears more irregular with respect to the DRE forced cases, in agreement with previous works [1,2,6]. This effect is related to the simultaneous development in the BL of multiple CFI wavelengths with varying initial amplitude, as well as to the spanwise local characteristics of the DRP patch, which may induce locally stronger or weaker CFI. The transition front location of the BL flow incurred by a set of DRP measured throughout this work is presented in Fig. 10(b). Despite the local geometrical features of the applied DRP, the forced flow scenario is comparable among cases, as also confirmed by the repeatability of the transition front location at fixed Re_{cx} and the outcome of the DRP characterization (Fig. 2). The mild residual data scatter observed in the extracted transition location can be attributed to the specific geometrical variations among the collection of applied DRP (Fig. 2).

Local characteristics of the BL flow incurred by the C7-D₈ forcing are investigated through the PTV acquisitions. Figures 11(a) and 11(b), presenting the \bar{w} and \bar{w}_d velocity contours, show

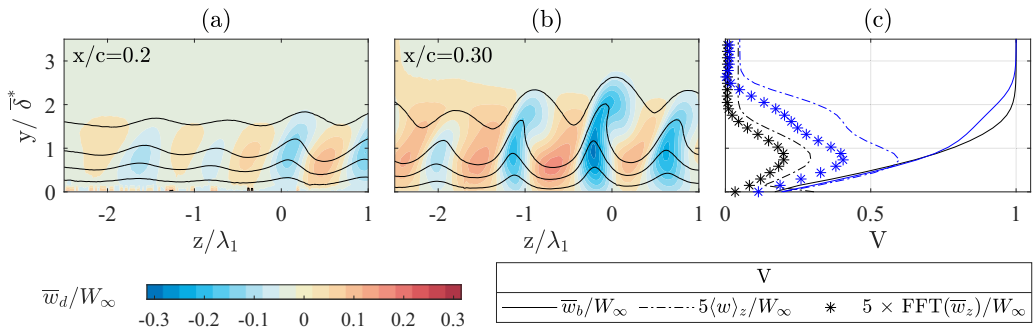


FIG. 11. Contours of \bar{w}_d at (a) $x/c = 0.2$ and (b) $x/c = 0.3$ for C7-D₈ forcing. Contours of \bar{w} every 20% W_∞ (black solid lines). (c) Comparison of \bar{w}_b (solid line), $\langle w \rangle_z$ (dot-dashed line), and λ_1 FFT shape function (*) at $x/c = 0.2$ (black lines) and $x/c = 0.3$ (blue lines).

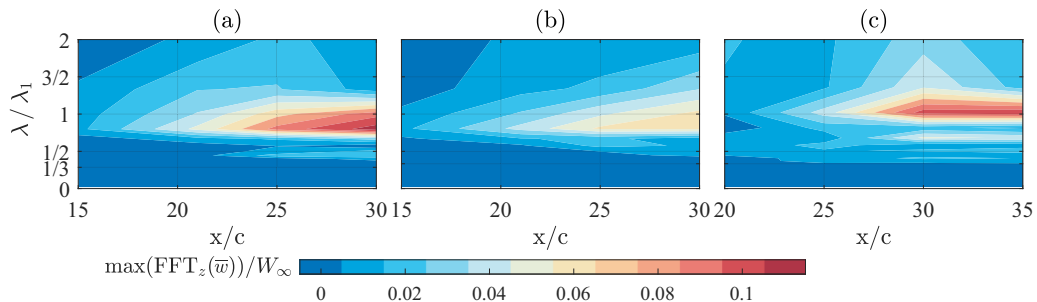


FIG. 12. Spatial FFT analysis: FFT spectra contours in the x - λ plane for case (a) C7-D₈, (b) C7-D₉, and (c) C7-D₁₃.

that the resulting BL velocity is significantly modulated, indicating the presence of well-developed CFI [19,20]. The early development of CFI in the considered case can be related to the vicinity of the C7-D₈ patch to the wing leading edge, which is the most receptive region to external flow disturbances [2,11]. Accordingly, Fig. 11(c) shows that at $x/c = 0.3$ the corresponding \bar{w}_b profile features an inflection point indicative of the mean flow deformation. Moreover, due to the local geometrical characteristics of C7-D₈, each of the identified crossflow vortices mildly differs from its neighbors either in strength, size, or stage of development. This can be related to the interaction of the multiple CFI modes excited by the DRP, as well as to the presence of individual peaks and valleys in the DRP patch. The latter induce CFI with higher or lower initial amplitudes, and consequently faster or slower development [6,21,23]. Furthermore, Fig. 11(c) exhibits the $\langle w \rangle_z$ profile extracted from the displayed flow fields. Similarly to the reference DRE forcing of Fig. 5, $\langle w \rangle_z$ is characterized by the presence of a secondary peak at $x/c = 0.3$, suggesting the presence of nonlinear interactions between the developing CFI modes.

The investigation of the BL spectral content is performed through the spanwise FFT, which results in the spectra reported in Fig. 12(a) for the representative C7-D₈ case. The chordwise spectra evolution confirms that the BL is still dominated by the λ_1 mode, as would be expected from predictions of stability theory for similar conditions [32,34]. Nonetheless, high spectral content is also associated with a wide range of wavelengths between $\lambda_1/3$ and $3/2\lambda_1$. This further motivates the nonlinear characteristics observed in the $\langle w \rangle_z$ evolution [Fig. 11(c)]. Comparable flow features are observed for other leading-edge DRP patches (i.e., C7-D₉), whose corresponding spectra are reported in Fig. 12(b). The lower CFI spectral amplitude measured in the latter case can be related to the mildly lower k_{DRP} of C7-D₉ [Fig. 2(a)].

Having demonstrated the repeatability of the DRP patches geometry (Sec. II C) and of BL flow features they induce, in the remainder of this work the DRP patch located at the leading edge is generically indicated as D_I . The CFI amplitudes induced by the representative D_I are reported in Figs. 13(a) and 13(b). In agreement with the spectral characteristics and the observed presence of nonlinearities, for the D_I forcing case, A_{int} [Fig. 13(a)] achieves significantly higher values than those computed for A_{int,λ_1} [Fig. 13(b)]. In particular, the λ_1 mode accounts for almost half of the total disturbance amplitude, while the evolution of the initiated set of small wavelength modes contributes for the remaining CFI amplitude. The relevant contribution of the developing set of CFI wavelengths is as well evident in the amplitude differences between the λ_1 FFT shape function and the $\langle w \rangle_z$ profile, enhanced at $x/c = 0.3$ due to the increased strength of the excited CFI modes. This behavior, as well as the overall amplitude values, are comparable between the various DRP patches measured (not reported for sake of conciseness), further confirming that the global flow features induced by the DRP are mostly independent from their local geometry.

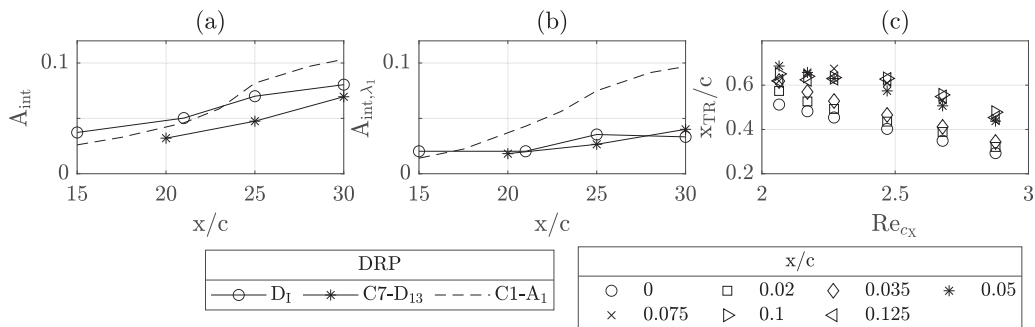


FIG. 13. Integral amplitude chordwise evolution for cases D_I, C7-D₁₃, and C1-A₁. (a) A_{int} ; (b) A_{int,λ_1} . (c) Transition front chordwise location at various Re_{c_x} for DRP patches starting at various x_{DRP}/c .

B. Effect of DRP chord location

As a final step for the DRP characterization, the sensitivity of the BL transition and of the developing CFI to x_{DRP} is investigated. In particular, DRP patches of 3% chord streamwise length are applied starting at various chord locations. The x_{TR} extraction for the considered cases shows that a downstream shift of the DRP starting location is accompanied by a downstream shift of transition [Fig. 13(c)]. Furthermore, the FFT analysis of the \bar{w}_d signal for a representative case C7-D₁₃ (with $x_{\text{DRP}}/c = 0.035$, indicated as D_{II} in the remainder of this work) is reported in Fig. 12(c). The spectral evolution confirms that the BL contains CFI modes corresponding to a range of wavelengths between $\lambda_1/3$ and $3/2\lambda_1$, with significant peaks for the λ_1 mode and its harmonics. Both the spectral peaks and the corresponding CFI amplitudes (reported in Fig. 13 for D_{II}) achieve mildly lower values with the x_{DRP} downstream shift. This agrees well with the observed downstream shift of the transition location, and it reflects the results obtained by the authors in a previous investigation dedicated to the BL receptivity to the DRE array location [35]. Nonetheless, also for the D_{II} case, the λ_1 mode amplitude only accounts for part of the total disturbance amplitude (A_{int}), as multiple CFI modes are simultaneously developing and interacting in the BL.

Overall, the dominant flow features incurred by the DRP appear to be repeatable among the various considered cases. As such, DRPs applied at the leading edge (i.e., D_I) or slightly downstream (i.e., D_{II}) are used as a baseline configuration to investigate the role and effectiveness of DRE arrays in BL affected by randomized roughness.

V. EFFECT OF DRE ARRAY SUPERPOSITION IN THE PRESENCE OF DRP

A. Effect of a reference DRE array superposition to a DRP patch

The characterization of the flow field induced by the sole DRP forcing confirms that the induced dominant flow features are repeatable among the various measured cases. Therefore, a reference DRE array is applied on the wing surface in combination with the DRP towards investigating the flow field resulting from the interaction between the velocity disturbances induced by the two roughness systems. In particular, reference arrays forcing the dominant λ_1 mode are applied in combination with D_I. The DIT image obtained by subtracting the flow field induced by D_I to the C8-D_I-A₁ configuration is reported in Fig. 14(a). With the addition of C8-A₁, the sawtooth pattern of the transition front appears more regular and uniform. However, both the DIT image as well as the extracted transition locations [Fig. 14(b)] indicate that the addition of a reference array forcing the dominant mode enhances the CFI development strongly advancing transition. This is the case for all forcing configurations reported in Fig. 14(b), in agreement with the results described by previous works for a 2D-BL [23,26]. Figure 14(c) reports a comparable investigation performed by adding the reference array to the BL forced by the more downstream DRP patch D_{II}. Despite the mildly

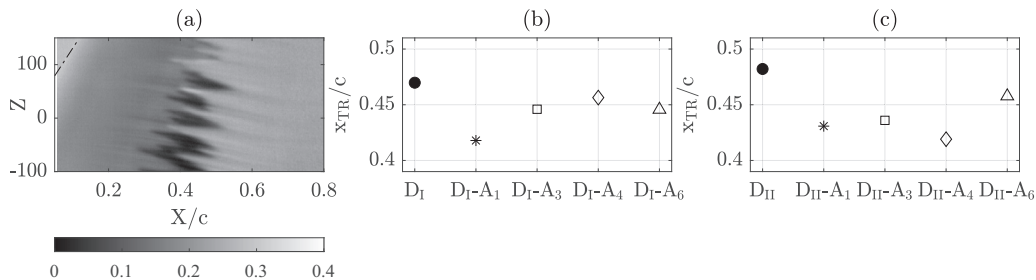


FIG. 14. (a) DIT image at $Re_{cx} = 2.17 \times 10^6$ computed subtracting the D_I case to $C8-D_I-A_1$. (b), (c) Transition front chordwise location at various Re_{cx} for cases (b) D_I , $C8-D_I-A_1$, $C8-D_I-A_3$, $C8-D_I-A_4$ and $C8-D_I-A_6$; and (c) $C8-D_{II}$, $C8-D_{II}-A_1$, $C8-D_{II}-A_3$, $C8-D_{II}-A_4$, and $C8-D_{II}-A_6$.

weaker CFI introduced by D_{II} , the application of the reference DRE array at any of the considered chord locations significantly advances the transition location. Case $D_{II}-A_4$ appears as an outlier in comparison to the general trend, possibly due to improper alignment of the DRE arrays.

This indicates once more that the dominant flow topology and the CFI downstream evolution are consistent for the various DRPs considered. However, the near-flow field induced by each DRP is expected to be locally affected by the geometrical features of the patches, particularly in the presence of peaks in the roughness distribution [19–22]. For the current investigation, this can lead to the formation of a near-DRP flow field that has a destructive interaction with the velocity disturbances introduced by the reference DRE array. Thus, the superposing velocity disturbance systems enhance the existing CFI instead of damping them, if the phase shift of the two disturbance systems is not suitably set.

Further quantification of the interaction between the flow structures induced by the DRP and DRE array is given by the FFT and amplitude analysis. The spanwise FFT spectra are reported in Fig. 15 for cases forced by D_I and a reference DRE array. The addition of the reference array enhances the development of the forced λ_1 mode, which rapidly overtakes the smaller wavelength modes introduced by D_I [Figs. 15(a) and 15(b)]. Consequently, the estimated A_{int} [Fig. 15(c)] rapidly reaches higher values in the presence of both DRP and DRE, motivating the recorded advancement in transition. In particular, configuration $C8-D_I-A_1$ forces the λ_1 mode on top of the D_I patch, thus introducing high initial amplitude CFI close to the highly receptive leading edge region [2, 11, 35]. This results in the rapid growth of the dominant stationary CFI and its harmonics, with the dominant CFI reaching amplitude saturation shortly after $x/c = 0.2$. Differently from what is observed for subcritical UFD configurations [5], the reported spectra indicate that despite the critical mode forcing applied, some residual small-wavelength modes remain present in the BL. This

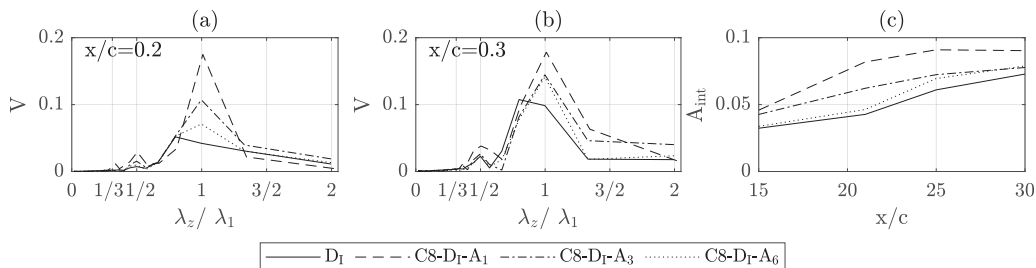


FIG. 15. Spatial FFT analysis: FFT spectra for $y/\delta^* = 1$ at (a) $x/c = 0.2$ and (b) $x/c = 0.3$ for cases D_I , $C8-D_I-A_1$, $C8-D_{II}-A_3$, and $C8-D_{II}-A_6$. V stands for $\max[\text{FFT}_z(\bar{w})]/W_\infty$. (c) Integral amplitude A_{int} computed for all cases.

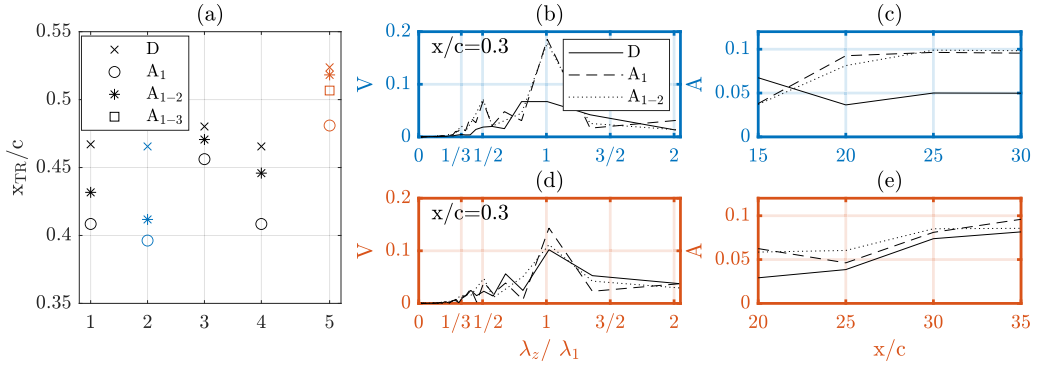


FIG. 16. (a) Transition front chordwise location at $Re_{cx} = 2.17 \times 10^6$ for cases 1. C8-D_I-A₁₋₂, 2. C8-D_I-A₄₋₅, 3. C8-D_{II}-A₇₋₈, 4. C9-D_I-A₁₋₂, and 5. C10-D_{II}-A₁₋₃. (b) FFT spatial spectra at $x/c = 0.3$ and $y/\delta^* = 1$ for cases C8-D_I-A₄₋₅ and (d) C10-D_{II}-A₁₋₃. V stands for $\max[\text{FFT}_z(\bar{w})]/W_\infty$. (c) A_{int} chordwise evolution for cases C8-D_I-A₄₋₅ and (e) C10-D_{II}-A₁₋₃.

can be related to the relatively high amplitude of the applied DRP, which excites a strong set of CFI (see also Sec. VB). Additionally, the lack of control on the phase shift between the DRP-induced CFI and the superposing disturbance systems introduced by the reference array may also affect the spanwise invariance of the resulting flow field. Nonetheless, despite resulting in enhanced CFI, in the case of a DRP-reference DRE forcing, most of the BL spectral energy is contained by the forced mode and its harmonics.

B. Effect of multiple DRE array superposition to DRP patches

As the superposition of the reference DRE array to the DRP leads to the development of more uniform albeit stronger CFI, the effect on the developing CFI of the addition of control DRE arrays is hereafter investigated. Forcing configurations comparable to the ones presented in Sec. III are measured in the presence of the DRP.

The BL transition location resulting from the superposition to a DRP patch of a set of two or more arrays (i.e., a reference and one or more control arrays) is shown in Fig. 16(a). Cases C8-D_I-A₁₋₂, C8-D_I-A₄₋₅, and C9-D_I-A₁₋₂ are applied in combination with D_I, while cases C8-D_{II}-A₇₋₈ and C10-D_{II}-A₁₋₃ are applied in combination with D_{II} (with reference to Table I). Both of the considered upstream array forcing cases (C8-D_I-A₁₋₂ and C9-D_I-A₁₋₂) feature a reference array with nominal height k_1 located on top of D_I. As previously observed, in such configurations the reference array induces the rapid development of a strong monochromatic λ_1 mode, enhancing the existing CFI [Figs. 16(b) and 16(c)]. The application of a control array successfully delays transition with respect to the BL forced by the superposition of D_I and the reference array [Fig. 16(a)]. The achieved transition delay is relatively mild for configuration C8-D_I-A₁₋₂, while it appears to be more significant for the case C9-D_I-A₁₋₂, featuring a control array with higher nominal amplitude k_2 . However, none of the three considered forcing configurations is strong enough to delay the transition location with respect to the sole D_I forcing. This can be related to the persistence in the BL of residual incoherent modes initiated by the DRP [Fig. 16(b)]. These modes accompany the development of the dominant λ_1 mode, enhanced by the DRE forcing. Consequently, the multiple DRE arrays technique demonstrates reduced cancellation capabilities in the presence of DRP.

The effect of the superposition of the more downstream patch and the multiple DRE arrays is also investigated. The C8-D_{II}-A₇₋₈ configuration shows comparable behavior to the previously described cases, while the C10-D_{II}-A₁₋₃ configuration appears to be more effective [Fig. 16(a)]. In particular, in the latter case the superposition of the velocity disturbance systems induced by D_{II}, the reference array C10-A₁ with nominal amplitude k_1 , and the control array C10-A₂ with nominal am-

plitude k_2 leads to a BL transition location comparable to that of the sole D_{II} forcing. Accordingly, the FFT [Fig. 16(d)] and amplitude [Fig. 16(e)] analysis of the incurred flow fields show comparable CFI evolution and behavior for the sole D_{II} and for the C10- D_{II} - A_{1-2} configuration. This effect can be related to the milder (possibly lower peak amplitude) patch applied in case C10- D_{II} , which results in the development of a weaker set of small-wavelength instabilities as confirmed by the more downstream transition location. Accordingly, the application of the reference DRE array focuses the CFI on the forced mode, but it is also more effective at damping the incoherent set of modes introduced by the DRP. This partially restores the cancellation capabilities of the proposed linear superposition technique. However, the addition of a second control array (C10- A_3) to the forcing configuration leads again to transition advancement. This effect is observed also in the presence of different DRP patches and with changes in the amplitude and location of the DRE arrays (results not reported for the sake of conciseness).

Overall, the multiple DRE forcing configuration proves to be less effective at canceling the CFI in the presence of the enhanced surface roughness, at least within the investigated parameter space. This is mostly attributed to the residual nonuniformity of the developing BL, which prevents the effective cancellation of the phase shift between the existing CFI (incurred by the DRP) and the velocity disturbances introduced by the applied DRE arrays. Consequently, the combined forcing given by the DRP and DRE roughness systems can enhance the existing CFI instead of damping them. Nonetheless, the application of a control array effectively delays the transition location with respect to the reference array-DRP forcing configuration. This indicates that further investigation of the proposed technique can lead to the development of a more robust design for the multiple DRE forcing applied in combination with the DRP. A possible expansion of the investigated parameter space can be insightful towards identifying more efficient configurations. Furthermore, the exploration of multiple DRE forcing based on subcritical arrays (i.e., UFD) can result in improved control capabilities, thanks to the combined effect of the nonlinear conditioning and of the linear superposition of velocity disturbances. Alternatively, the wing surface can be equipped with sensors in order to sense the incoming CFI actual phase and location on the wing, thus tuning the cancellation technique to the proper antiphase. As an example, this could be achieved by employing smart morphing surfaces, protruding membranes, or microplasma actuators [13,46].

VI. CONCLUSIONS

This work presents a cancellation technique aiming at damping the CFI introduced by a reference DRE array by applying a streamwise series of optimally designed control arrays. All the DRE arrays applied throughout this work force the most unstable CFI mode for the present conditions, and they are arranged with suitable DRE amplitude and spanwise phase shifts. This allows for investigating whether linear superposition of the introduced velocity systems is sufficient to cancel CFI in the considered scenario. The presented flow fields are measured by IR thermography and planar PTV acquisitions, respectively, allowing for the characterization of the BL laminar-to-turbulent transition location and for the quantification of the local BL development.

The successive application of multiple critical control DRE arrays on a smooth wing surface (i.e., $R_q = 0.2 \mu\text{m}$ and an average height of $5 \mu\text{m}$) leads to significant damping of the monochromatic CFI introduced by a reference array. Accordingly, the transition location shifts up to 8% chord more downstream with respect to the sole reference array forcing case. The observed transition delay is comparable to results obtained through subcritical DRE forcing on a smooth wing [8]. The cancellation capabilities of a multiple DRE configuration appear to be robust to the mild changes of Re_{cx} considered in this investigation. Nonetheless, the effectiveness of the cancellation strongly depends on the multiple array configuration design parameters (i.e., DRE height, chordwise spacing, and chord location). The spanwise spatial FFT analysis confirms the forced λ_1 mode dominates the BL development both in the sole reference array forcing as well as with the addition of successive control arrays. In the latter configuration, the amplitudes of the dominant stationary CFI and of its harmonics are both significantly decreased, reducing the mean flow modulation and

the nonlinearities affecting the BL development. The fact that the dominant CFI wavelength is left unaltered by the array superposition further confirms that the introduced technique is based on the linear superposition of the velocity disturbance systems introduced by each of the applied DRE arrays. Given the demonstrated capabilities of DRE arrays in canceling a preexisting monochromatic CFI, the discussed technique can be brought forward towards realistic spanwise-regular transition scenarios, for example to mitigate the effect of CFI introduced by a set of rivets protruding from the wing surface.

However, the cancellation capabilities of the proposed method are found to be significantly reduced by the presence of enhanced distributed surface roughness, similar to the effect of a rough wing surface finishing (i.e., $k_{\text{DRP}} \simeq 0.12 \mu\text{m}$). This behavior is comparable with previous experimental observations dedicated to subcritical forcing applied in enhanced surface roughness scenarios [11]. In the presented work, randomized distributed surface roughness is simulated by applying multiple DRP patches obtained by spraying adhesive on the wing surface. These patches contain a random distribution of geometrical peaks, initiating a set of CFI with statistically dispersed wavelengths and phases. Accordingly, the resulting BL is still dominated by the most unstable stationary mode λ_1 , but it also contains a set of CFI modes with wavelengths between $\lambda_1/2$ and $3/2\lambda_1$.

In these cases, the application of a reference DRE array succeeds in partially focusing the developing CFI on the forced λ_1 mode, albeit resulting in a transition front advancement. However, the developing BL still suffers from residual spanwise nonuniformity due to the persistence of the weaker CFI modes induced by the DRP. This appears to be one of the main limitations of the proposed technique, partly attributable to the choice of forcing the critical CFI mode rather than the $2/3\lambda_1$ mode typically employed in subcritical forcing and UFD investigations. As a consequence, the application of successive DRE arrays in this configuration proves to be more challenging from a design perspective, as well as less effective in canceling the preexisting CFI. More specifically, the addition of control arrays successfully delays the transition location with respect to the flow field incurred by the DRP-reference array combination. Nonetheless, in all of the configurations measured throughout the current investigation, the superposition of multiple DRE arrays to the DRP patch results in a reduced (or unchanged) extent of the laminar flow region with respect to the sole DRP forcing. This can be related to the lack of control on the location and phase shift between the preexisting CFI, introduced by the DRP-reference array combination, and the velocity disturbances induced by the applied control DREs.

In conclusion, the proposed technique effectively cancels CFI on a smooth wing surface. The obtained transition delay corresponds to a potential extension of laminar flow of about 8% chord, providing a significant drag reduction opportunity. However, the actual potential for the application of the proposed cancellation technique is limited by its strong sensitivity to the external disturbance environment, especially the enhanced distributed surface roughness considered throughout this study. Therefore, further investigation will be necessary to fully understand and control the mechanisms dominating DRP and DRE superposition. In particular, the superposition of the velocity disturbances appears to be significantly sensitive to the design parameters of the applied DRE arrays. Hence, the expansion of the investigated parameter space can prove helpful towards identifying more robust roughness designs. One of the main limitations of the presented technique is the lack of control on the phase shift between the preexisting and the introduced velocity disturbances. This results in the presence of residual small-wavelength CFI modes in the DRP-reference DRE forced boundary layer, which is detrimental for the effectiveness of the control arrays. Towards overcoming this limit, the forcing of subcritical CFI modes (both for the reference and control arrays) should be investigated as an effective alternative, possibly combining the effect of the subcritical control (UFD) and of the linear superposition of velocity disturbances. Additionally, similarly to the adapted systems developed for TS and CFI cancellation, the implementation of active flow control techniques capable of monitoring and actively actuating the spanwise location of the developing CFI disturbances and their phase content can be investigated. At the current state of development, the applied reference array is not sufficient to effectively impose the location and

phase of the CFI initiated by the DRP. An active control technique could then be used to establish these parameters, such that the location and spanwise phase shift of the reference and control arrays can be suitably adjusted to achieve the desired destructive interference between the existing CFI and the superposing disturbance systems.

ACKNOWLEDGMENTS

The authors are grateful to the European Research Council for financially supporting this research through the GLOWING Starting Grant (803082).

-
- [1] H. Bippes, Basic experiments on transition in three-dimensional boundary layers dominated by crossflow instability, *Prog. Aeronaut. Sci.* **35**, 363 (1999).
 - [2] W. Saric, H. Reed, and E. White, Stability and transition of three dimensional boundary layers, *Annu. Rev. Fluid Mech.* **35**, 413 (2003).
 - [3] J. Serpieri and M. Kotsonis, Three-dimensional organisation of primary and secondary crossflow instability, *J. Fluid Mech.* **799**, 200 (2016).
 - [4] M. Malik, F. Li, M. Choudari, and C. Chang, Secondary instability of crossflow vortices and swept-wing boundary-layer transition, *J. Fluid Mech.* **399**, 85 (1999).
 - [5] P. Wassermann and M. Kloker, Mechanisms and passive control of crossflow-vortex-induced transition in a three-dimensional boundary layer, *J. Fluid Mech.* **456**, 49 (2002).
 - [6] R. H. Radeztsky Jr., M. Reibert, and W. Saric, Effect of isolated micron-sized roughness on transition in swept-wing flows, *AIAA J.* **37**, 1370 (1999).
 - [7] M. Reibert, W. Saric, J. Carrillo, and K. Chapman, Experiments in nonlinear saturation of stationary crossflow vortices in a swept-wing boundary layer, in *34th Aerospace Sciences Meeting and Exhibit, Reno, NV* (American Institute of Aeronautics and Astronautics, Reston, VA, 1996).
 - [8] W. Saric, J. Ruben Carrillo, and M. Reibert, Leading-edge roughness as a transition control mechanism, in *36th AIAA Aerospace Sciences Meeting and Exhibit, Reno, NV* (American Institute of Aeronautics and Astronautics, Reston, VA, 1998).
 - [9] A. Carpenter, W. Saric, and H. Reed, Roughness receptivity in swept-wing boundary layers—experiments, *Int. J. Eng. Syst. Modell. Simul.* **2**, 128 (2010).
 - [10] M. Woodruff, W. Saric, and H. Reed, Receptivity measurements on a swept-wing model, in *41st AIAA Fluid Dynamics Conference and Exhibit, Honolulu, Hawaii* (American Institute of Aeronautics and Astronautics, Reston, VA, 2011).
 - [11] W. Saric, D. West, M. Tufts, and H. Reed, Experiments on discrete roughness element technology for swept-wing laminar flow control, *AIAA J.* **57**, 641 (2019).
 - [12] P. Wassermann and M. Kloker, DNS-investigations of the development and control of crossflow vortices in a 3-d boundary-layer flow, in *Laminar-Turbulent Transition* (Springer, Berlin, 2000), pp. 565–570.
 - [13] R. Messing and M. J. Kloker, Investigation of suction for laminar flow control of three-dimensional boundary layers, *J. Fluid Mech.* **658**, 117 (2010).
 - [14] T. Friederich and M. J. Kloker, Control of the secondary cross-flow instability using localized suction, *J. Fluid Mech.* **706**, 470 (2012).
 - [15] R. W. Milling, Tollmien–schlichting wave cancellation, *Phys. Fluids* **24**, 979 (1981).
 - [16] H. W. Liepmann, G. L. Brown, and D. M. Nosenchuck, Control of laminar-instability waves using a new technique, *J. Fluid Mech.* **118**, 187 (1982).
 - [17] M. Kotsonis, R. Giepmans, S. Hulshoff, and L. Veldhuis, Numerical study of the control of tollmien–schlichting waves using plasma actuators, *AIAA J.* **51**, 2353 (2013).
 - [18] H. J. Tol, C. C. de Visser, and M. Kotsonis, Experimental model-based estimation and control of natural tollmien–schlichting waves, *AIAA J.* **57**, 2344 (2019).
 - [19] J. M. Kendall, Laminar boundary layer velocity distortion by surface roughness: Effect upon stability, AIAA paper **195**, 1981 (1981).

- [20] E. Reshotko and L. Leventhal, Preliminary experimental study of disturbances in a laminar boundary layer due to distributed surface roughness, in *14th Fluid and Plasma Dynamics Conference, Palo Alto, CA* (American Institute of Aeronautics and Astronautics, Reston, VA, 1981).
- [21] R. S. Downs, III, E. White, and N. Denissen, Transient growth and transition induced by random distributed roughness, *AIAA J.* **46**, 451 (2008).
- [22] S. Drews, R. Downs, C. Doolittle, D. Goldstein, and E. White, Direct numerical simulations of flow past random distributed roughness, in *49th AIAA Aerospace Sciences Meeting Including the New Horizons Forum and Aerospace Exposition, Orlando, Florida* (American Institute of Aeronautics and Astronautics, Reston, VA, 2011).
- [23] S. D. Drews, Direct numerical simulations of flow past quasi-random distributed roughness, M.Sc. thesis, The University of Texas at Austin, Austin, TX, 2012.
- [24] J. R. Dagenhart and W. S. Saric, Crossflow stability and transition experiments in swept-wing flow, NASA Center (1999).
- [25] A. Sharma, S. Drews, M. S. Kuester, D. B. Goldstein, and E. B. White, Evolution of disturbances due to distributed surface roughness in laminar boundary layers, in *52nd Aerospace Sciences Meeting, National Harbor, Maryland* (American Institute of Aeronautics and Astronautics, Reston, VA, 2014).
- [26] M. S. Kuester and E. B. White, Roughness receptivity and shielding in a flat plate boundary layer, *J. Fluid Mech.* **777**, 430 (2015).
- [27] A. R. Berger, M. N. McMillan, E. B. White, S. Suryanarayanan, and D. B. Goldstein, Suppression of transition behind a discrete roughness element using a downstream element, in *Tenth International Symposium on Turbulence and Shear Flow Phenomena* (Begel House, 2017).
- [28] S. Suryanarayanan, D. B. Goldstein, A. R. Berger, E. B. White, and G. L. Brown, Mechanisms of roughness-induced boundary-layer transition control by shielding, *AIAA J.* **58**, 2951 (2020).
- [29] H. Kurz and M. Kloker, Mechanisms of flow tripping by discrete roughness elements in a swept-wing boundary layer, *J. Fluid Mech.* **796**, 158 (2016).
- [30] Aero, *Quarterly Issue: Issue 49 Quarter 01*, Tech. Rep. (Boeing, 2013), https://www.boeing.com/commercial/aeromagazine/articles/2013_q1/pdf/AERO_2013q1.pdf.
- [31] J. Serpieri and M. Kotsonis, Design of a swept wing wind tunnel model for study of cross-flow instability, in *33rd AIAA Applied Aerodynamics Conference, Dallas, TX* (American Institute of Aeronautics and Astronautics, Reston, VA, 2015).
- [32] J. Serpieri, Cross-flow instability, Ph.D. thesis, Delft University of technology, Delft, NL, 2018.
- [33] A. Rius-Vidales and M. Kotsonis, Influence of a forward-facing step surface irregularity on swept wing transition, *AIAA J.* **58**, 5243 (2020).
- [34] L. Mack, Boundary-layer linear stability theory, Tech. Rep. (California Inst of Tech Pasadena Jet Propulsion Lab, 1984).
- [35] G. Zoppini, S. Westerbeek, D. Ragni, and M. Kotsonis, Receptivity of crossflow instability to discrete roughness amplitude and location, *J. Fluid Mech.* **939**, A33 (2022).
- [36] G. Zoppini, T. Michelis, D. Ragni, and M. Kotsonis, The near-wake of discrete roughness elements on swept wings: tomographic ptv measurements, in *12th International Symposium on Turbulence and Shear Flow Phenomena (TSFP12), Osaka, Japan* (2022).
- [37] M. Brynjell-Rahkola, P. Schlatter, A. Hanifi, and D. Henningson, Global stability analysis of a roughness wake in a falkner-skan-cooke boundary layer, *Proc. IUTAM* **14**, 192 (2015).
- [38] W. Saric, A. Carpenter, and H. Reed, Passive control of transition in three-dimensional boundary layers, with emphasis on discrete roughness elements, *Philos. Trans. R. Soc. London A* **369**, 1352 (2011).
- [39] O. Reynolds, On the extent and action of the heating surface of steam boilers, *Papers on Mechanical and Physical Subjects* 81 (1901).
- [40] J. Lemarechal, M. Costantini, C. Klein, M. J. Kloker, W. Würz, H. B. Kurz, T. Streit, and S. Schaber, Investigation of stationary-crossflow-instability induced transition with the temperature-sensitive paint method, *Exp. Therm. Fluid Sci.* **109**, 109848 (2019).
- [41] A. Rius-Vidales, M. Kotsonis, A. Antunes, and R. Cosin, Effect of two-dimensional surface irregularities on swept wing transition: Forward facing steps, in *2018 Fluid Dynamics Conference, Atlanta, Georgia* (American Institute of Aeronautics and Astronautics, Reston, VA, 2018).

- [42] M. Raffel, C. Merz, T. Schwermer, and K. Richter, Differential infrared thermography for boundary layer transition detection on pitching rotor blade models, *Exp. Fluids* **56**, 30 (2015).
- [43] L. Hunt and W. Saric, [Boundary-layer receptivity of three-dimensional roughness arrays on a swept-wing](#), *41st AIAA Fluid Dynamics Conference and Exhibit, Honolulu, Hawaii* (American Institute of Aeronautics and Astronautics, Reston, VA, 2011), p. 3881.
- [44] D. Tempelmann, L. Schrader, A. Hanifi, L. Brandt, and D. Henningson, Swept wing boundary-layer receptivity to localized surface roughness, *J. Fluid Mech.* **711**, 516 (2012).
- [45] R. S. Downs, III and E. White, Free-stream turbulence and the development of cross-flow disturbances, *J. Fluid Mech.* **735**, 347 (2013).
- [46] T. Friederich and M. Kloker, Control of crossflow-vortex induced transition: DNS of pinpoint suction, in *41st AIAA Fluid Dynamics Conference and Exhibit, Honolulu, Hawaii* (American Institute of Aeronautics and Astronautics, Reston, VA, 2011).